

Max-Cut graph-driven quantum circuit design for planar spin glasses

Seyed Ehsan Ghasempouri*

Department of Chemistry, University of New Brunswick, Fredericton, New Brunswick E3B 5A3, Canada

Gerhard W. Dueck†

Faculty of Computer Science, University of New Brunswick, Fredericton, New Brunswick E3B 5A3, Canada

Stijn De Baerdemacker‡

*Department of Chemistry, University of New Brunswick,
Fredericton, New Brunswick E3B 5A3, Canada and*

Department of Mathematics and Statistics, University of New Brunswick, Fredericton, New Brunswick E3B 5A3, Canada

(Dated: April 17, 2025)

Finding the ground state of spin glasses is a challenging problem with broad implications. Many hard optimization problems, including NP-complete problems, can be mapped, for instance, to the Ising spin glass model. We present a graph-based approach that allows for accurate state initialization of a frustrated triangular spin-lattice with up to 20 sites that stays away from barren plateaus. To optimize circuit efficiency and trainability, we employ a clustering strategy that organizes qubits into distinct groups based on the maximum cut technique, which divides the lattice into two subsets maximally disconnected. We provide evidence that this Max-Cut-based lattice division offers a robust framework for optimizing circuit design and effectively modeling frustrated systems at polynomial cost. All simulations are performed within the variational quantum eigensolver (VQE) formalism, the current paradigm for noisy intermediate-scale quantum (NISQ), but can be extended beyond. Our results underscore the potential of hybrid quantum-classical methods in addressing complex optimization problems.

I. INTRODUCTION

Determining the ground state of an Ising spin glass [1], a problem within the class of combinatorial optimization, becomes exponentially challenging for classical computers as the system size increases, similar to other many-body problems. Quantum computers, first proposed in the early 1980s [2–4], are anticipated to surpass these limitations by leveraging quantum mechanical phenomena, including superposition, interference, and entanglement. This advancement in quantum computing offers significant potential for solving specific computational challenges. Two of the most prominent algorithms in this field are the quantum phase estimation (QPE) [5–9] and the variational quantum eigensolver (VQE) [10, 11]. The QPE algorithm typically requires a high circuit depth to accurately determine the ground state energy, which necessitates further development in error-corrected hardware. Consequently, the VQE, a quantum-classical hybrid approach with shallow circuit depth, is a viable alternative for noisy intermediate-scale quantum (NISQ) devices [12]. However, this advantage comes at the cost of potentially encountering an NP-hard optimization problem during the training process [13]. The objective of the VQE is to find a parameterized ansatz that can determine the energy of the target state or provide a reasonable quantum state estimation for the QPE. The ansatz

is prepared by designing a quantum circuit with a variational form, consisting of layers that specify rotation patterns and CNOT gates. One of the most challenging aspects of VQE is the design of an efficient variational quantum circuit with shallow depths, which is crucial in noisy environments and demands a minimal number of parameters to avoid issues related to barren plateaus and entrapment in local minima.

The Ising problem has a tight connection with optimization problems. The Quantum Approximate Optimization Algorithm (QAOA), introduced by Farhi, Goldstone, and Gutmann in 2014 [14], is an optimization algorithm based on the VQE method designed to address combinatorial problems. The QAOA has been widely studied to solve quadratic unconstrained binary optimization (QUBO) problems [15, 16] such as Maximum Cut (Max-Cut) [14, 17], Maximum Independent Set (MIS) [18], Binary Paint Shop Problem (BPSP) [19], Binary Linear Least Squares (BLLS) [20], etc. The QAOA method has many scientific and industrial applications such as portfolio optimization [21], tail assignment [22], protein folding [23], etc. In several situations, such as QUBO, the QAOA can be mapped to the problem of finding the ground state of an Ising system.

Exploring the ground-state properties of Ising spin glasses stands as a key difficulty in both solid-state physics and statistical mechanics and has been extensively researched for many decades [24–27]. The term spin glass denotes a state of disordered magnetism where the spins of magnetic atoms or molecules interact in such a way that it gives rise to frustrated magnetic phenomena [28]. The behavior of frustrated magnetic metals

* ehsan.ghasempouri@unb.ca

† gdueck@unb.ca

‡ stijn.debaerdemacker@unb.ca

is observed in alloys such as CuMn and AuFe, where manganese (Mn) or iron (Fe) is introduced as impurities into copper (Cu) or gold (Au) [29, 30]. The Ising model is widely used due to its simplicity and effectiveness in capturing the essential features of real spin glasses, as it accounts for the interaction energy between impurities [31, 32]. The presence of unsatisfied edges in the lattice can lead to situations where multiple geometric arrangements of atoms remain stable. For a spin glass with n spins, there are 2^n possible configurations, making the task of finding the ground state a combinatorial problem. It has been shown that for planar graphs with nearest-neighbor interactions, both with and without periodic boundary conditions, and in the absence of an external magnetic field, the ground state can be found in polynomial time [33–38] and is comparable to solving the Max-Cut problem. However, Barahona proved that computing the ground state energy for two-dimensional (2D) models with a magnetic field is NP-hard, even without periodic boundary conditions, and no polynomial algorithm exists for this problem [32].

Over the past few decades, various methods, such as Monte Carlo simulations [39] and evolutionary algorithms [40, 41], including genetic algorithms [42], have been developed to determine the ground state energy of Ising spin glasses. However, these approaches generally provide only approximations rather than the exact ground state, with a significant limitation that there is no guarantee of finding the true ground state [31, 43]. Additionally, another major drawback of these heuristic methods is their performance in the presence of degeneracies. Two states with almost identical energy levels can still be qualitatively different. Therefore, even though these algorithms can give energies close to the ground state, they may not be close to the true ground state. As a result, these methods are inadequate for analyzing real ground states, such as those found in protein folding applications, as mentioned in reference [44]. An alternative approach to finding the true ground state involves adiabatic methods, such as simulated annealing (SA) [45], quantum annealing (QA) [46], and the quantum adiabatic algorithm (QAA) [47]. The SA method is an optimization technique that seeks the ground state by simulating a system gradually cooling into a low-energy state. The downside of this method is that the cooling process must be prolonged; otherwise, the system may get trapped in local minima rather than reaching the global minimum. The QA relies on quantum fluctuations and aims to find optimal solutions by gradually reducing an applied transverse magnetic field to the spin system at the lowest possible temperature. Experiments [48] and simulations [49, 50] have demonstrated that QA can achieve equilibrium in a spin glass more rapidly than SA, which operates through thermal annealing. However, removing the magnetic field reduces quantum fluctuations and forces the system to pass through the critical point. A complete understanding of the transition between the disordered phase, which occurs at large fields, and the

spin glass phase, which emerges at smaller fields, is still lacking and remains an active area of research. A recent study [51] utilizing extreme-scale simulations, primarily based on Monte Carlo methods, demonstrated that it is possible to reach the quantum spin-glass phase with an annealing time that scales polynomial in the number of qubits, provided that parity-changing excitations are avoided. One possible limitation of this optimistic outlook is that simply crossing the critical point differs from navigating through the entire bulk glass phase to reach the final state at zero transverse-field, which may still be challenging [52]. The QAA is closely related to the QA but is specifically a Hamiltonian-based quantum algorithm where the Hamiltonian undergoes slow evolution, enabling the system to remain in its ground state. Determining the complexity of the QAA is crucial, particularly when the minimum of the first excitation gap (ΔE_{min}) is small, since the total evolution time (τ) is inversely related to ΔE_{min} . If ΔE_{min} becomes exponentially small at any point during the evolution, the simulation time can grow exponentially, rendering the QAA inefficient [53]. The same issue arises in QA as well, since it also requires adiabatically transitioning from the critical point to a vanishing magnetic field. The complexity of this task becomes even more problematic in higher dimensions [54–56]. Given the limitations of adiabatic approaches, exploring alternative methods is important. For instance, an algebraic approach has been proposed for designing a quantum circuit that efficiently diagonalizes the Ising Hamiltonian and provides access to all eigenstates by directly preparing the computational basis states. This approach has been applied to a 4-qubit system and holds the potential for extension to larger qubit numbers; however, only for the one-dimensional Ising model [57, 58]. Recently, a promising study [59] demonstrated the effectiveness of noise-mitigation techniques in quantum simulations of a 2D transverse-field Ising model implemented on a 127-qubit heavy-hexagon lattice. The results surpassed those of several classical tensor network methods applied to the same problem, even when the classical approaches utilized substantial computational resources. In addition, in a recent advance, King et al. [60] used a large-scale, programmable quantum annealer to analyze entanglement growth in spin glasses, demonstrating area-law scaling in quench dynamics across two-, three-, and infinite-dimensional topologies. They showed that state-of-the-art classical methods based on tensor and neural networks could not match the quantum annealer’s accuracy within a reasonable timeframe.

Finding the ground state of an Ising spin glass falls within a specific subset of NP-hard problems known as NP-complete. This class of problems has a notable property: if an algorithm is found that can efficiently solve any NP-complete problem, it will make a wide range of hard optimization problems within this subset easy to solve. Therefore, developing an efficient algorithm to solve the spin glass Hamiltonian and determine its min-

imum energy could have far-reaching implications. Such an algorithm would enable solutions to various challenging combinatorial problems, including the traveling salesman problem and protein folding [61–63]. These problems, among others, can be formulated using the Ising spin glass model. The broader problem-solving potential that comes with determining the ground state of Ising spin glasses is the key motivator driving researchers from diverse disciplines to tackle this challenge. For instance, the Hopfield model [64], along with other groundbreaking neural network models, uncovered significant links between neural networks and Ising spin glasses across general networks [65–67]. A range of deep neural network architectures, including generative models [68–74] and reinforcement learning [75, 76], have been applied to solve Ising models. Designing neural networks to solve the Ising spin glass model on larger and more complex graphs can not only open the door for the development of powerful optimization tools but also illuminate the limitations and boundaries of deep-learning-assisted algorithms [74].

In this study, we aim to simulate a frustrated system consisting of a triangular spin lattice up to 20 sites and utilize the VQE method to compute the energy. We will demonstrate that the Max-Cut realization of the lattice provides an excellent guideline for dividing the lattice into two distinct groups and establishing connections between them.

The following sections of the paper are structured as outlined below. We begin by discussing the spin glass theory and simulating the triangle transverse-field Ising model, which represents the simplest frustrated system and serves as a building block for the triangular lattice, using the cluster circuit based on the Max-Cut method. In the subsequent section, we extend our approach to simulate frustrated systems with 5 and 7 sites, as well as a 10-site triangular lattice. Finally, we explore the potential applications of the proposed method to predict the magnetic behavior of larger lattices, up to 20 sites. All simulations were performed in the Qiskit environment [77], and details are available in the Supporting Information.

II. SPIN GLASS

For the triangular spin lattice depicted in Figure 1, the Hamiltonian takes the following form:

$$H = - \sum_{i,j} J_{ij} Z_i Z_j. \quad (1)$$

In this context, the summation over i,j includes all sites on the lattice, with J_{ij} being the coupling constant. Here, Z_i represents the spin operator at site i . For $J_{ij} < 0$ we have an antiferromagnetic interaction. Since the building block of this lattice is a triangle, it results in frustrated interactions. For the antiferromagnetic Ising (AF) model on a triangle, only two of the spins can align in an

antiparallel manner, resulting in six degenerate ground states. See Figure 2.

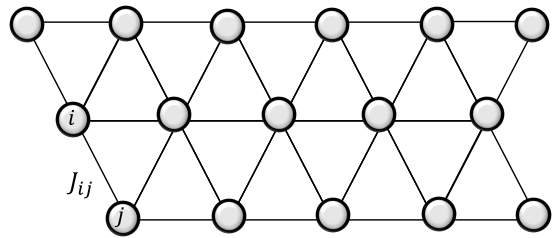


FIG. 1. A triangular spin lattice with J_{ij} nearest-neighbor interactions.

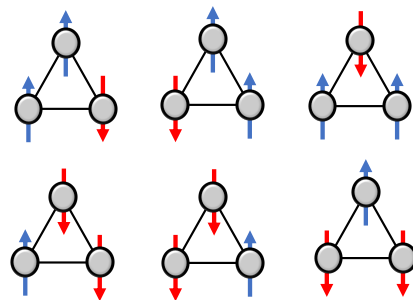


FIG. 2. AF Ising spins on a triangle.

In 1973, Anderson proposed the resonating valence bond (RVB) approach [78] to determine the ground state of a triangular lattice (spin glass). In this method, we treat the system pairwise, considering each pair of spins as a valence bond (VB) formed between two antiferromagnetic spins. Due to the multiple ways that sites can pair, we must consider a superposition of VB states (Figure 3). Consequently, we encounter a combinatorial problem because of the many possible ways to choose these pairs, and the system may exhibit various forms of resonance, complicating the consideration of interactions between magnetic sites.

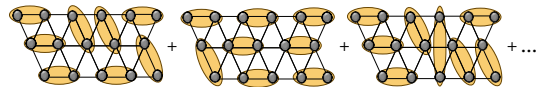
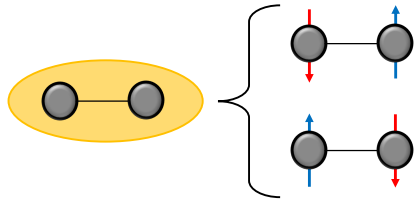


FIG. 3. Superposition of possible VB states .

For $2w$ site we have $(2w)!/(2^w w!)$ unique pairing. As demonstrated in our previous work[79], designing a quantum circuit based on the RVB approach does not require considering all possible pairs to obtain the true ground state. Identifying only the key pairings is sufficient to reach the desired state. In small magnetic systems like a cyclic hexagon, the important resonances between pairs are represented as benzene Kekulé or Dewar structures. However, as systems grow larger, pinpointing the significant pairings becomes progressively more challenging.

Moreover, in the context of quantum circuits, accounting for all possible pairings can exponentially increase circuit depth, which is inefficient for quantum devices. Therefore, a guideline is necessary to help determine which pairings should be considered for accurately simulating the target state.



$$|\psi_{pair}\rangle = \frac{1}{\sqrt{2}} \{ |\downarrow\uparrow\rangle - |\uparrow\downarrow\rangle \}. \quad (2)$$

The breakdown of a RVB pair into an alternating spin-up/down suggests a bipartite coloring scheme. If we assign red to spin-down and blue to spin-up, the entire graph can be divided into two distinct colors. Each edge that connects nodes of different colors is in line with the antiferromagnetic nature and is called satisfied. There is no pairing between two sites that share the same color (Figure 4), and we speak of an unsatisfied edge.

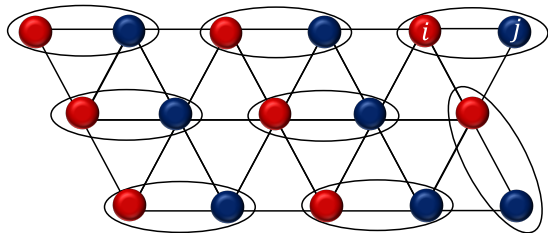


FIG. 4. A triangular spin lattice is divided into different colors based on the spin of each pair. The red color represents spin-down, while the blue color represents spin-up.

A key observation is that the graph with the maximum number of edges between two color groups would have the fewest unsatisfied edges, leading to the most stable classical configuration. Finding such a clustering to minimize unsatisfied edges is equivalent to solving the Max-Cut problem, which aims to maximize the number of edges between different colors. Therefore, we use the Max-Cut approach as a guideline to determine the optimal pairings and design a quantum circuit accordingly. We note that polynomially solvable algorithms for planar graphs exist [80–82]. Earlier works on 2D Ising spin glasses with random Gaussian interactions on a square lattice already employed maximum weight cuts to find the ground states [31, 43] energy on classical hardware. Later on, [39] investigated the harder problem where random interactions are replaced by $\pm J$ in which the sign of each bond is random but its magnitude is fixed. With the branch-and-cut algorithm described there, a 100×100 grid can be handled, however, it is hard to predict the

running time, and for larger lattices, it is challenging to find the exact result in polynomial time. The goal of this study is to employ Max-Cut as an effective guideline to find efficient quantum circuits. Throughout this work, we use a fixed sign for the interaction term $J_{ij} < 0$.

A. Transverse-Field Ising Model and Max-Cut

The general form of the transverse-field Ising model is

$$H = -J_{ij} \sum_{i,j} Z_i Z_j - h \sum_i X_i, \quad (3)$$

where (X_i, Y_i, Z_i) represent the Pauli spin matrices at lattice site i , J_{ij} denotes the nearest-neighbor magnetic interaction along the z -axis, and h represents the magnetic field in the x -direction. A single triangle is the simplest frustrated system, so we will simulate the antiferromagnetic transverse-field Ising model on a triangular system using the Max-Cut method, offering a clear and efficient starting point.

The goal of the Max-Cut problem is to divide the vertices of a graph into two distinct sets so as that maximize the edges that connect them. To label the two different groups, we can assign binary digits, 0 and 1. It is important to note that we cannot cut an edge that connects nodes within the same group. To solve the Max-Cut problem, we aim to maximize a specific cost function, which can be defined as follows

$$f(\vec{x}) = \sum_{i,j=0}^{n-1} w_{ij} x_i (1 - x_j), \quad (4)$$

w_{ij} represents the weight of the edge between nodes i and j , and $\vec{x} = (x_0, x_1, \dots, x_{n-1}) \in \mathbb{B}^n$, where $\mathbb{B} = \{0, 1\}$ is a binary vector with a length corresponding to the number of nodes in the graph. Due to the graph being undirected, the weights are such that w_{ij} is equal to w_{ji} . Assigning a spin site s_i to each vertex (V), where the spin value is $s_i = \pm 1$, allows us to categorize the graph into two sets: vertices with spin-up (V^+) and vertices with spin-down (V^-). In the context of quantum computing, where we measure the expectation value of observables composed of Pauli operators, the connection to spin lattice mapping is logical and coherent. Indeed, this task can be accomplished by making the following assignment:

$$x_i = (1 - Z_i)/2, \quad (5)$$

where Z_i denotes the Pauli Z operator that has eigenvalues ± 1 . This change of variable implies that

$$\begin{aligned} x_i = 0 &\rightarrow Z_i = 1, \\ x_i = 1 &\rightarrow Z_i = -1. \end{aligned} \quad (6)$$

Upon employing equation (5) and substituting it into equation (4), we obtain

$$f(\vec{z}) = \sum_{i=0}^{n-1} \sum_{j=0}^i \frac{w_{ij}}{2} - \sum_{i=0}^{n-1} \sum_{j=0}^i \frac{w_{ij}}{2} Z_i Z_j. \quad (7)$$

Furthermore, the intrinsic inclination of a quantum computer is to seek minima, typically the lowest energy, rather than maxima. Therefore, instead of maximizing $f(\vec{z})$, we aim to minimize

$$-f(\vec{z}) = \sum_{i,j=0}^{n-1} \frac{w_{ij}}{2} Z_i Z_j - \sum_{i,j=0}^{n-1} \frac{w_{ij}}{2}. \quad (8)$$

The observable for which we will calculate the expectation value is

$$H = \sum_{i=0}^{n-1} \sum_{j=0}^i \frac{w_{ij}}{2} Z_i Z_j, \quad (9)$$

with a constant correction.

In statistical physics and disordered systems, the Max-Cut problem is analogous to minimizing the Hamiltonian of an Ising spin glass without an external magnetic field. This reduces equation (3) to the following form

$$H = -J_{ij} \sum_{i,j} Z_i Z_j. \quad (10)$$

Utilizing the QAOA Algorithm [14] we can initially leverage a quantum computer to identify the maximum cut in an arbitrary graph. However, we use a more heuristic approach here, given the relatively small size of the system ($n \leq 20$).

B. Hamiltonian and symmetries

It is straightforward to verify that the transverse-field Ising model Hamiltonian commutes with the total-spin flip operator

$$X = \prod_{i=1}^N X_i. \quad (11)$$

The proof boils down to showing that all local $Z_i Z_j$ commute with X . We get

$$\begin{aligned} [X, Z_i Z_j] &= \prod_{k \neq i,j} X_k [X_i X_j, Z_i Z_j] \\ &= \prod_{k \neq i,j} X_k (X_i Z_i X_j Z_j - Z_i X_i Z_j X_j) \\ &= \prod_{k \neq i,j} X_k ((-iY_i)(-iY_j) - (iY_i)(iY_j)) \\ &= 0. \end{aligned} \quad (12)$$

As a result, eigenfunctions of the Hamiltonian must also be eigenfunctions of the X operator. Due to the idempotency of the X operator ($X^2 = 1$), a \mathbb{Z}_2 symmetry arises, with eigenvalues ± 1 corresponding to the symmetric (+) and antisymmetric (-) sectors. The eigenstates of the X operator exhibit a special property: any two states

with the maximum Hamming distance exhibit equal amplitude. However, their phases may vary. For example, in the two-qubit case, the eigenstates take the following form

$$|v^\pm\rangle = \frac{1}{\sqrt{2}} (|00\rangle \pm |11\rangle), \quad (13)$$

$$|w^\pm\rangle = \frac{1}{\sqrt{2}} (|01\rangle \pm |10\rangle). \quad (14)$$

Consequently, a linear combination of symmetric states, $|v^+\rangle + |w^+\rangle$, or antisymmetric states, $|v^-\rangle + |w^-\rangle$, is also an eigenstate of the X operator. Thus, the general form of the eigenstates can be rewritten as follows

$$|M^\pm\rangle = \cos x |v^\pm\rangle + \sin x |w^\pm\rangle. \quad (15)$$

Furthermore, $|M^\pm\rangle$ spans all states of the two-site Hamiltonian ($H_{2\text{-site}}$). Introducing the dimensionless parameters a, b with $a \in [0, 1]$ and $b = 1 - a$ into Hamiltonian (3), where $J_{ij} = -b$ and $h = -a$ (definitions that are used consistently throughout the paper for other n -site systems), the two-site antiferromagnetic Hamiltonian ($H_{2\text{-site}}$) becomes

$$H_{2\text{-site}} = bZ_1 Z_0 + a(X_0 + X_1). \quad (16)$$

The state $|M^+\rangle$ is the ground state in the second and fourth quadrants, with $\tan \frac{x}{2} = \frac{-b - \sqrt{4a^2 - b^2}}{2a}$, and the highest excited state in the first and third quadrants, with $\tan \frac{x}{2} = \frac{-b + \sqrt{4a^2 + b^2}}{2a}$. Thus we have

$$H_{2\text{-site}} |M^+\rangle = \begin{cases} +\sqrt{b^2 + 4a^2} |M^+\rangle, & x \in \text{QI or QII} \\ -\sqrt{b^2 + 4a^2} |M^+\rangle, & x \in \text{QIII or QIV} \end{cases} \quad (17)$$

Where QI-QIV denote the four quadrants. Similarly, $|M^-\rangle$ includes the first and second excited states, with $x = \frac{\pi}{2}$ yielding the first excited state $|v^-\rangle$ and $x = 0$ the second excited state $|w^-\rangle$. It is important to note that $|M^-\rangle$ is not an eigenstate of $H_{2\text{-site}}$ in general. However, it preserves the form of $|M^-\rangle$ through its action :

$$H_{2\text{-site}} |M^-\rangle = b(\cos x |v^-\rangle - \sin x |w^-\rangle). \quad (18)$$

Preserving the form means the output state retains equal amplitudes for maximally Hamming distant states, with possible phase differences. This property arises from the commutation of the Ising Hamiltonian with the X operator. By leveraging these properties, one can search for the target state using a quantum circuit within a confined searching space aligned with the target state's structure. This reduction is important as it addresses one of the primary sources of barren plateaus during cost landscape optimization [83].

In the next section, we introduce the fundamental building block for designing a quantum circuit inspired by the symmetry of the system's Hamiltonian and explain the partitioning mechanism using the Max-Cut approach for a single triangle.

C. Circuit building block and single triangle

Here, we present the fundamental circuit component for generating nearest-neighbor interactions, referred to as two-qubit cluster (2-qc).

$$\boxed{2\text{-qc}} = \begin{array}{c} \bullet \\ | \\ \oplus \\ \text{---} \\ \oplus \\ \bullet \end{array} \text{---} \boxed{R_y(\theta)} \text{---} \begin{array}{c} \bullet \\ | \\ \oplus \\ \text{---} \\ \oplus \\ \bullet \end{array} \quad (19)$$

This component is designed to align with the symmetry of the system's Hamiltonian and represents the partitioning mechanism using a cut for the simplest two-site system. The 2-qc operator ($U_{2\text{-qc}}$) with qubit i controlling j can be written as

$$\text{CNOT} \cdot R_Y(2\theta) \cdot \text{CNOT} = \cos \theta I - i \sin \theta Y_j Z_i. \quad (20)$$

Interestingly, the $U_{2\text{-qc}}$ commute with the X operator [$X, U_{2\text{-qc}}] = 0$, because,

$$X_i X_j [\cos \theta I - i \sin \theta Y_j Z_i] X_i X_j = \cos \theta I - i \sin \theta Y_j Z_i. \quad (21)$$

The consequence of this is that as soon as a reference state is an eigenstate of the X operator

$$X|\psi\rangle = (\pm)|\psi\rangle, \quad (22)$$

acting with whatever $U_{2\text{-qc}}$ operator on the reference state will remain in the same symmetry sector.

$$XU_{2\text{-qc}}|\psi\rangle = U_{2\text{-qc}}X|\psi\rangle = (\pm)U_{2\text{-qc}}|\psi\rangle. \quad (23)$$

So, a circuit consisting of any 2-qc gates will be an eigenstate of the X provided the reference state $\prod_i |q_i\rangle$ is an eigenstate of X . The reference (or initial) state $|\pm\rangle^{\otimes n}$ can be easily prepared as an eigenstate of the X operator by applying an $R_y(\theta)$ gate to each qubit with $\theta = \pm \frac{\pi}{2}$. Furthermore, noting that $U_{2\text{-qc}}$ provides an exact eigenstate for the 2-spin system. Applying $U_{2\text{-qc}}$ to $|M^\pm\rangle$ preserves its form, as can be shown

$$U_{2\text{-qc}}|M^\pm\rangle = \cos(x \pm \frac{\theta}{2})|v^\pm\rangle + \sin(x \pm \frac{\theta}{2})|w^\pm\rangle. \quad (24)$$

The next step is generalizing the circuit design approach for representing a graph with n nodes. As a showcase, we first simulate the single triangle, where two edges are cut based on Max-Cut (see Figure (5))

In the following, we demonstrate how the exact ground state can be constructed from the Max-Cut for the triangle.

Considering the circuit (19), where the rotation gate acts on the target qubit, there are two options for each individual edge in Max-Cut. For clarity, we define each node in the graph as a control or source (s) qubit, or as a target or sink (t) qubit. The graph represents this relationship with a green arrow, starting from the s node

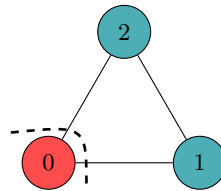
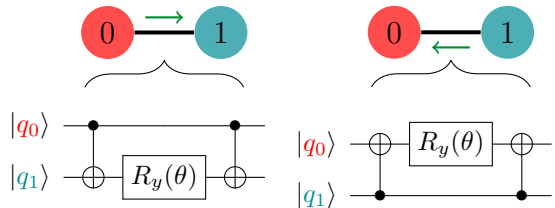


FIG. 5. The graph is divided into red and cyan clusters, with the dashed line indicating the maximum cut.

and pointing to the t node. For example, for a single edge, we have:



In the graph, each node belongs to one of two distinct color sets, red or cyan. We define a subcircuit s , where all nodes in the same set act as control qubits, and a subcircuit t , where all nodes in the same set act as target qubits. Following this coloring scheme, we use the red nodes to build the quantum circuits. Together, the final circuit consists of two layers: one with the red nodes as s and the other with the red nodes as t . Additionally, since the circuit begins in the vacuum state, rotation gates are added at the start for initialization. The complete circuit for the triangle case is shown in Figure 6. We also define a mean-field circuit or Cut(0), which lacks any two-qubit interaction gates and excludes the s and t layers. By comparing the results with the mean-field circuit, we can evaluate the percentage of recovered correlation energy. The following two considerations are worth mentioning related to the design of the subcircuits, s and t . First, within each subcircuit (s or t), the two distinct 2-qc blocks are commutative, as the rotation gate acts solely on the target qubit. This property ensures that the output state remains unchanged regardless of the sequence of 2-qc blocks, thus eliminating combinatorial choices about block placement in the circuit. The second, perhaps less obvious, consideration is the order of the subcircuits s and t : does it matter which comes first? As we will demonstrate, the answer is no. Swapping s with t merely shifts the cost function landscape. While this property may be less critical than the first, in larger systems (where repeating the s and t blocks is necessary), the design's flexibility highlights the effectiveness of the proposed circuit as a viable alternative.

We extend the observation of Equation (24) by repeatedly applying the $U_{2\text{-qc}}$ block to the n -qubit case, where the qubits involved in the 2-qc block within the subcircuit act as either s or t . As a result of Equation (23), the symmetry is always preserved.

We now provide the mathematical proof demonstrating the capability of the circuit in Figure 6 to reproduce the

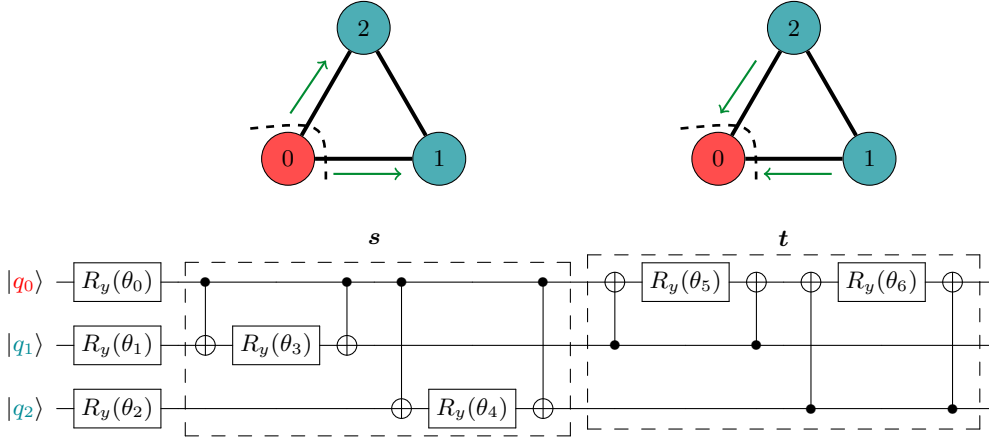


FIG. 6. The whole circuit for the AF Ising spins on a triangle

exact target state. The triangular Ising model has $2^3 = 8$ possible configurations. We can categorize the possible configurations based on the number of unsatisfied edges, where both sites on an edge have the same spin. In total, there are two different classes of configurations: those with one unsatisfied edge (1U class) and those with three unsatisfied edges (3U class). The latter case represents a less favorable state due to its higher energy. The general wavefunction has the following form:

$$|\psi\rangle = N \left(\sum_{i=0}^1 p_i |P_i\rangle + \sum_{j=0}^5 q_j |Q_j\rangle \right), \quad (25)$$

TABLE I. Labeling scheme for $|P_i\rangle$ and $|Q_i\rangle$ states, categorized into 3U and 1U classes.

Class	Label	Basis State
3U	$ P_0\rangle$	$ 000\rangle$
	$ P_1\rangle$	$ 111\rangle$
1U	$ Q_0\rangle$	$ 001\rangle$
	$ Q_1\rangle$	$ 010\rangle$
	$ Q_2\rangle$	$ 011\rangle$
	$ Q_3\rangle$	$ 100\rangle$
	$ Q_4\rangle$	$ 101\rangle$
	$ Q_5\rangle$	$ 110\rangle$

where N is the normalization factor, $|P_i\rangle$ and $|Q_j\rangle$ represent 3U and 1U classes respectively. p_i and q_j represent the amplitudes corresponding to configurations in each class. Those configurations in the same class have equal amplitudes in terms of magnitude. This equality results from their symmetry and balanced contribution to the wavefunction, where none of the configurations is more stable than the others, making them equally significant. However, the phase of the amplitudes for the same class can vary. We can denote the magnitudes of amplitudes for classes 3U and 1U as $\cos\theta$ and $\sin\theta$, respectively, leveraging their equivalence in absolute amplitudes within the same class. Consequently, the normalization

factor can be determined as follows:

$$|p_0| = |p_1| = \cos\theta, \quad |q_0| = |q_1| = \dots |q_5| = \sin\theta, \quad (26)$$

$$N = \frac{1}{\sqrt{2(2 - \cos 2\theta)}}. \quad (27)$$

Similar to the two-site case, we can demonstrate the ground state based on the eigensates of the X operator using the labeling scheme in Table I. The eight eigenstates of the X operator are:

$$|v_0^\pm\rangle = \frac{1}{\sqrt{2}} (|P_0\rangle \pm |P_1\rangle), \quad (28)$$

$$|v_1^\pm\rangle = \frac{1}{\sqrt{2}} (|Q_5\rangle \pm |Q_0\rangle), \quad (29)$$

$$|v_2^\pm\rangle = \frac{1}{\sqrt{2}} (|Q_4\rangle \pm |Q_1\rangle), \quad (30)$$

$$|v_3^\pm\rangle = \frac{1}{\sqrt{2}} (|Q_2\rangle \pm |Q_3\rangle). \quad (31)$$

The basis set $\{|v_i^\pm\rangle\}$ spans all states of the Hamiltonian. The proper phase for each basis state in constructing the ground state is determined by examining its expectation energy in the general form across all possible phase assignments. We omit these details for brevity and instead focus on the ground state, which serves as our target state. It can be shown explicitly that the target state $|\psi_{\text{tgt}}\rangle$ has the following form

$$|\psi_{\text{tgt}}\rangle = \frac{1}{\sqrt{2 - \cos 2\theta}} \left(\cos\theta |v_0^-\rangle - \sin\theta \sum_{i=1}^3 |v_i^-\rangle \right), \quad (32)$$

where the angle θ satisfies

$$\tan \theta = \frac{(2b + a) + 2\sqrt{a^2 + ab + b^2}}{3a}, \quad (33)$$

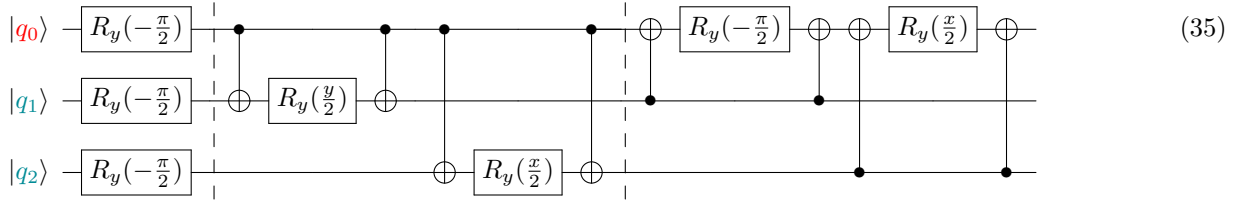
and the ground-state energy is given by

$$E_{\text{tgt}} = -a + b - 2\sqrt{a^2 + ab + b^2}. \quad (34)$$

Each configuration in the target state is characterized by a sign determined by the number of spin-up and spin-

down sites. Configurations with an odd number of 1's are assigned a minus sign, whereas those with an even number of 1's have a plus sign. For instance, $|001\rangle$ holds a minus sign, whereas $|110\rangle$ carries a plus sign. Therefore, if two different configurations have a maximum Hamming distance, they should exhibit opposite signs with respect to each other.

As we can see, the target state consists of two coefficients, implying that only one parameter is required to obtain it. To maintain consistency, the circuit in Figure 6 reproduces the desired state using a single parameter, for all a and b values as shown below.



where $\tan(\frac{y}{2}) = \sqrt{2} \sin(x + \pi/4)$, resulting in the output state:

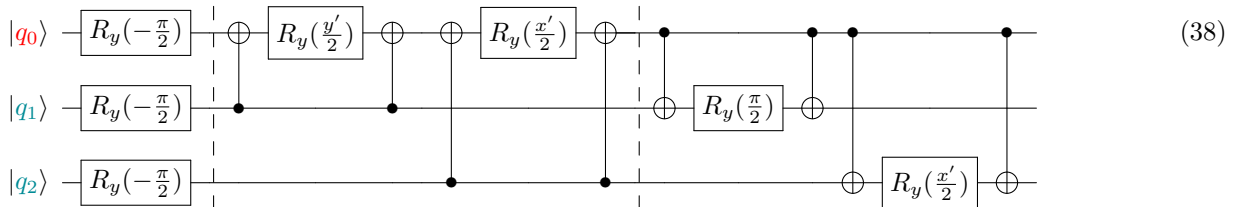
$$\psi_{s-t} = C \left((2 \sin x + \cos x) |v_0^-\rangle + \cos x \sum_{i=1}^3 |v_i^-\rangle \right), \quad (36)$$

here $s-t$ represents a single layer of subcircuit s and subcircuit t , with the order of s and t proceeding from left to right and $C = \frac{1}{\sqrt{2(2+\sin(2x))}}$. By applying the

identity $\tan x = \frac{1-\cot \theta}{2}$, one can derive Equation 32. In this context, the variable x satisfies the following relation:

$$\tan x = \frac{-(a+b) + \sqrt{a^2 + ab + b^2}}{a}. \quad (37)$$

As mentioned earlier, we can swap subcircuits s and t to obtain the target state, and we derive:



where $y' = 2 \tan^{-1}(\sqrt{2} \sin(x' - \pi/4))$, resulting in the output state:

$$\psi_{t-s} = C' \left(\sin(x' + \frac{\pi}{4}) |v_0^-\rangle + \cos(x' + \frac{\pi}{4}) \sum_{i=1}^3 |v_i^-\rangle \right), \quad (39)$$

here $C' = \frac{1}{\sqrt{2-\sin(2x')}}$. By using the identity $\tan(x' + \frac{\pi}{4}) = -\cot \theta$, Equation 32 can be derived. This leads to the following relationship between x' and the pa-

rameters a and b of the Hamiltonian:

$$\tan x' = \frac{-(a+2b) + 2\sqrt{a^2 + ab + b^2}}{a}. \quad (40)$$

For larger systems, we will apply the 2-qc building block to benchmark the trainability of the circuit in finding the target state. The capability of this framework to find the target state for larger frustrated systems is explored in the following section. Whereas the Max-Cut was able to reproduce the ground state for the triangle exactly, this is no longer the case for larger graphs. How-

ever, taking the triangle as building blocks for frustrated systems, one can employ the s and t circuits in the same vein.

D. 5-site frustrated Ising model

Here, we present results for a 5-site frustrated Ising model on the house graph [84]. For various cuts, including Max-Cut to evaluate the circuit's performance across different graph partitioning approaches (see Figure 7). To distinguish between different cuts, we define $\text{cut}(\alpha)$, where α denotes the number of edges in a cut. In this case, the Max-Cut corresponds to $\text{cut}(5)$. In each scenario, the circuit starts from the initial state and employs three layers of s , t , and s subcircuits in the order of $s - t - s$. The resulting recovered correlation energy and state fidelity are presented in Figure 8. The Recovered Correlation Energy (RCE) is computed using the following equation:

$$\%RCE = \frac{E_{\text{mf}} - E_{\text{cut}}}{E_{\text{mf}} - E_{\text{tgt}}} \times 100, \quad (41)$$

where E_{mf} represents the mean-field expected energy obtained from the circuit outcome using only rotation R_y gates, without incorporating any 2-qubit gates or $\text{cut}(0)$. E_{cut} denotes the expected energy associated with a specific cut, while E_{tgt} represents the target state energy. The state fidelity (F) for each output state, corresponding to a cut with density matrix ρ_{cut} and the target state ρ_{tgt} , is defined as

$$F(\rho_{\text{cut}}, \rho_{\text{tgt}}) = \text{Tr} \left[\sqrt{\sqrt{\rho_{\text{cut}}} \rho_{\text{tgt}} \sqrt{\rho_{\text{cut}}}} \right]^2. \quad (42)$$

All simulations are conducted on a classical simulator using the estimator primitive from Qiskit Aer, without quantum shot noise and hardware errors. The sequential least-squares programming (SLSQP) [85] library was used as the classical optimizer.

Figure 8 demonstrates that the Max-Cut circuit achieves the exact solution with high fidelity across the entire interval of a . However, for $\text{cut}(4)$ and $\text{cut}(4^*)$, the exact result is reproduced only when $a \geq 0.5$, and as a decreases, the fidelity drops rapidly. As previously stated, simulating spin glasses becomes particularly challenging when the magnetic field is weak. Consequently, if the circuit provides an incomplete representation compared to the target state, it will readily align with the structure of an excited state. This leads to convergence to a linear combination of the ground state and the excited state, rather than the ground state itself.

The performance of the proposed method has been benchmarked against the QAOA [14] and ADAPT-VQE approaches [86] (see details about the methods in Appendix A). We analyzed the RCE and state fidelity relative to the exact results for $a = 0.1$, where the first excitation gap is 1.5×10^{-4} . The results are presented in

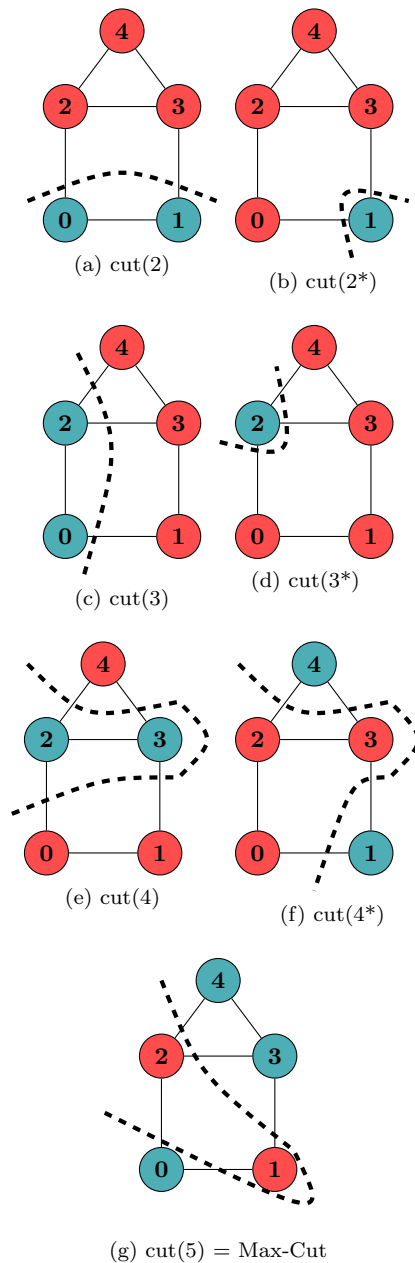
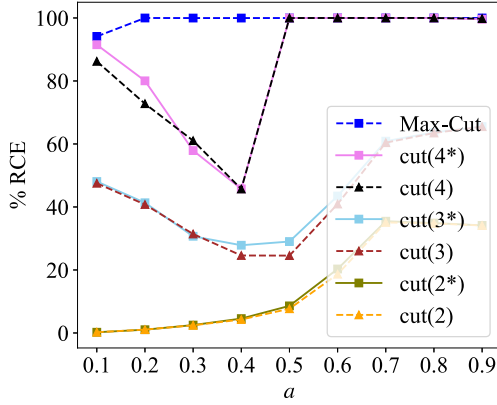
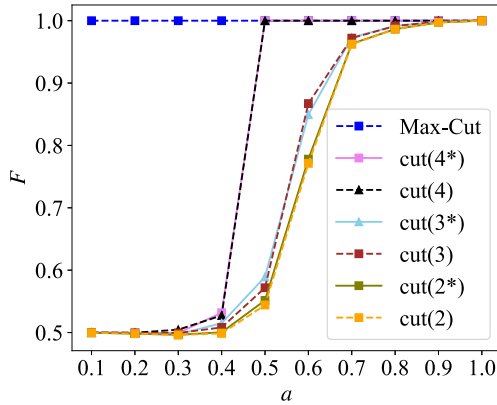


FIG. 7. Six possible cuts for the 5-site house configuration, including the Max-Cut.

Table II and visualized in Figure 9. As shown in the results, for a small value of a , the QAOA method requires a large number of layers to achieve accurate energy and wave function results. However, even with a depth of 310, the QAOA circuit does not reach a fidelity of 1.000 and exhibits a higher energy error compared to the Max-cut method. For ADAPT-VQE, a gradient threshold of 10^{-5} is required to achieve a fidelity of 1.000. However, with a gradient threshold of 10^{-4} , it is possible to obtain accurate energy results, with an energy error lower than that of the proposed method, but at the cost of poor state fidelity. Using very small gradient thresholds



(a)



(b)

FIG. 8. Comparison of the recovered correlation energy for different cuts, including the Max-Cut (a), and the state fidelity (b) for the 5-site house frustrated Ising model.

increases the circuit depth and also raises the number of measurements required for the operators in the pool. This example illustrates that the Max-Cut circuit can achieve accurate results with the highest fidelity while significantly reducing circuit complexity, requiring only one-tenth the depth of the QAOA circuit and one-fifth that of the ADAPT-VQE (see Figure 9).

E. 7 and 10-site frustrated Ising model

To further evaluate the capability of the Max-Cut circuit, the lattice size was increased to 7 and 10 sites to determine the number of source and sink layers required to achieve accurate results for %RCE and F within a . The term Max-Cut $_m$ is used to denote m layers of red nodes acting as sources and sinks. To obtain the Max-Cut, we use Equation (10) and set $J_{ij} = 1$ to assign equal weight to all edges in the graph. We then apply the QAOA algorithm to find the bitstrings (states) with the highest

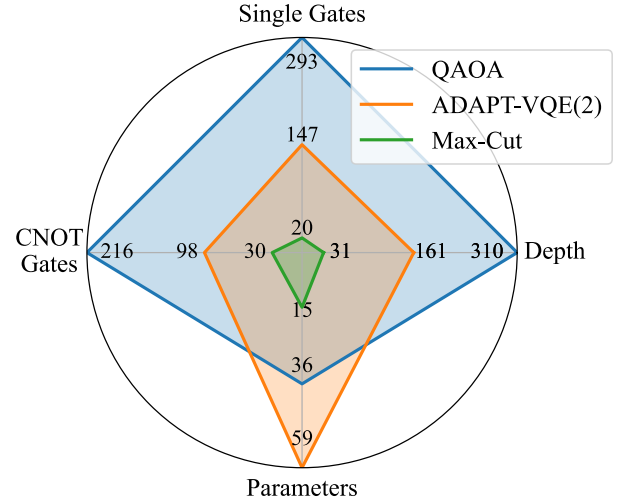


FIG. 9. Comparison of the circuit complexity between QAOA, ADAPT-VQE(2), and the Max-Cut circuit introduced in this work for the frustrated 5-site house Ising model with $a = 0.1$.

probabilities in the output of the QAOA circuit. These states represent the Max-Cut solutions.

Figure 10 illustrates a representative Max-Cut configuration among the four distinct solutions obtained for the 7-site hexagon graph using. The corresponding results are shown in Figure 11, indicating that an accurate solution corresponds to Max-Cut $_3$.

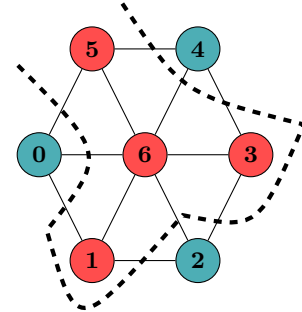
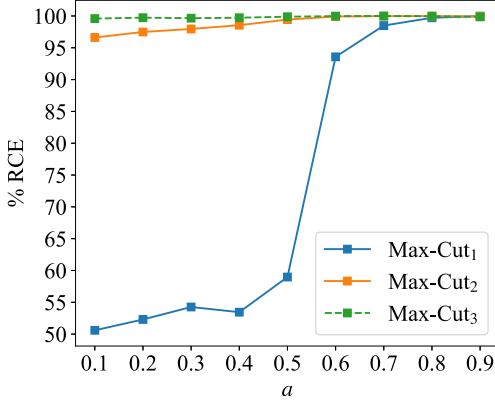


FIG. 10. One possible Max-Cut for the 7-site hexagon graph.

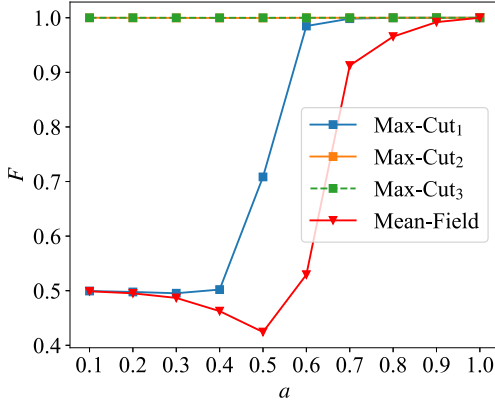
For the 10-site ribbon lattice, one possible Max-Cut configuration was obtained using the QAOA algorithm from a set of six distinct solutions, together with an alternative configuration (Figures 12 and 13). The simulation was carried out according to the configuration shown in Figure 12, while a comparison between the two Max-Cut solutions, including the results for the alternative configuration, is provided in the Appendix B. Interestingly,

TABLE II. Comparison of energy error, %RCE and F between QAOA, ADAPT-VQE, and the Max-Cut circuit introduced in this work for the frustrated 5-site house Ising model with $a = 0.1$.

Method	Energy Error	%RCE	Fidelity	Gradient Threshold
QAOA	0.01495	-721.4	0.954	-
ADAPT-VQE(1)	0.00008	95.6	0.500	10^{-4} (4 iterations)
ADAPT-VQE(2)	0.00000	100	1.000	10^{-5} (5 iterations)
Max-Cut	0.00006	96.4	1.000	-



(a)



(b)

FIG. 11. Comparison of the recovered correlation energy for different m shown in (a), and the state fidelity presented in (b) for the 7-site hexagon frustrated Ising model.

$m = 3$ once again provides a result with high state fidelity and accurate energy, as shown in Figure 14.

In Table III, %RCE and F compared with QAOA and ADAPT-VQE for $a = 0.1$, where the first excitation gap is 2.861×10^{-8} . For the QAOA method, 100 layers of problem and mixer Hamiltonians were utilized [14]. However, as evident from the table, despite this substantial number of repetitions, the state fidelity remains very

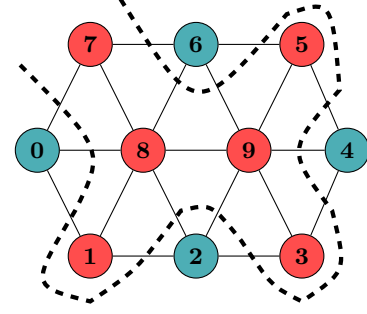


FIG. 12. One of the six possible Max-Cut solutions for the 10-site ribbon graph

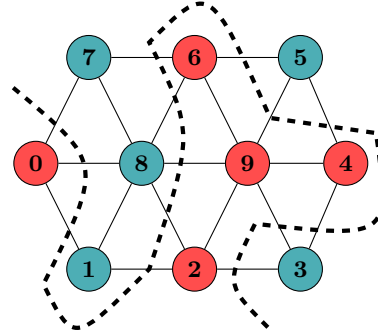


FIG. 13. Alternative Max-Cut configuration for the 10-site ribbon graph.

poor, and the energy error is significant. Due to the extremely small first excitation gap, achieving accurate results would require repeating the layers an excessively large number of times, leading to an exponential increase in circuit depth and the number of CNOT gates. On the other hand, the ADAPT-VQE method provides accurate energy estimates. However, with a gradient threshold of 10^{-4} , the state fidelity is not satisfactory, as this configuration results in a circuit with substantial depth and an excessive number of parameters. Consequently, obtaining an output state with high fidelity using ADAPT-VQE becomes challenging without significantly reducing the gradient threshold. Lowering the threshold further would produce a circuit that is both extremely deep and heavily parameterized, making it impractical. Table IV illustrates a comparison of circuit complexity scaling from a

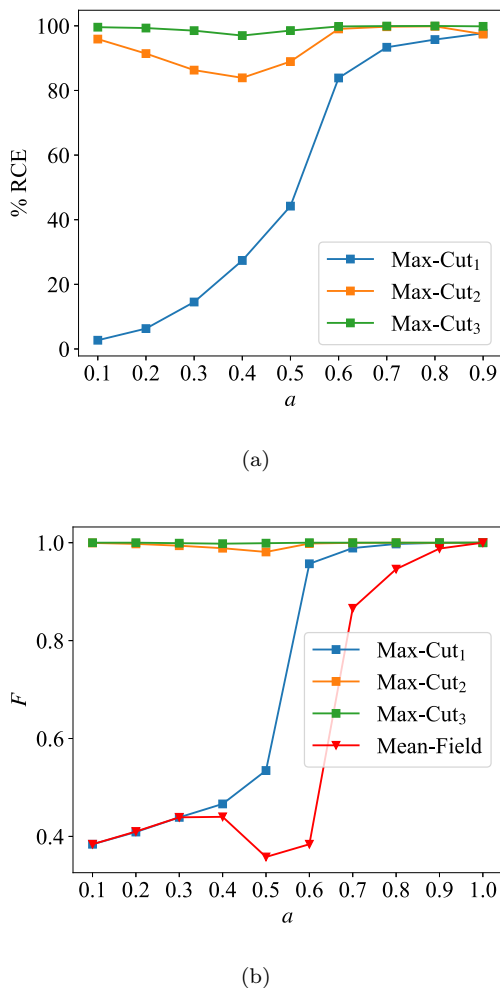


FIG. 14. Comparison of the recovered correlation energy for different m shown in (a), and the state fidelity presented in (b) for the 10-site ribbon frustrated Ising model.

5-site to a 10-site system for the Max-Cut circuit, QAOA, and ADAPT-VQE with $a = 0.1$. As observed, the circuit depth for the QAOA method increases significantly, yet the fidelity remains very poor. For the ADAPT-VQE approach, the scaling is approximately linear, similar to our method; however, the fidelity for the 10-site system is poor, and both the circuit depth and the number of parameters are significantly higher. Notably, the circuit depth for the 10-site system using our method is still lower than the depth required for the 5-site system with the ADAPT-VQE method.

In the following section, to evaluate the scalability of the proposed method for larger lattices and to verify whether $m = 3$ continues to provide a high-fidelity output state, we extend the lattice size to 20 sites.

F. 19 & 20-site frustrated Ising model

We applied the same procedure to simulate a lattice with 20 sites, corresponding to a Hilbert space dimension of $\dim \mathcal{H} \simeq 10^6$. One possible Max-Cut configuration, selected from forty solutions obtained using QAOA as the initial step in the circuit design, is shown in Figure 15. Due to the lack of symmetry in this lattice, compared to the previous lattices, it serves as a useful test for evaluating the capability of the Max-Cut circuit. We started from $a = 1$ and employed adiabatic optimization. For $m = 3$ and $m = 4$, the results are shown in Figure 16, and Table V presents the circuit complexity for.

The results indicate that $m = 3$ is adequate to reproduce the target state with high fidelity across nearly the entire interval of a . However, the energy error can be further reduced by increasing m to 4. Figure 17 highlights the robustness of the Max-Cut circuit in achieving high fidelity, by illustrating the first excitation gap obtained from the exact solution for different lattice sizes across the entire range of the magnetic field parameter a . Despite the fact that the first excitation gap decreases exponentially with increasing lattice size in the weak-field regime, as shown in Figure 17, the Max-Cut circuit demonstrates remarkable robustness by consistently maintaining high fidelity.

G. Correlation functions

Although energy and fidelity provide a good measure of the performance of the method, correlation functions $\langle Z_i Z_j \rangle$ are better probes as they can be obtained experimentally. We continue evaluating the performance of the circuit with $m = 3$ to analyze the correlation function $\langle Z_i Z_j \rangle$ and the magnetization $\langle X_i \rangle$, comparing them with the exact results. Calculations were performed for $a = 0.1$, which corresponds to the most challenging regime, by evaluating all possible interactions across all sites on the obtained output state and comparing them with the exact results. Figure 18 presents the correlation function for the exact results, while Figure 19 illustrates the differences with the simulation results. The results indicate that the error in the correlation function is small on average; however, larger deviations of up to $|\pm 0.115|$ are observed for interactions involving sites 16, 17, and 18. Consistently, by analyzing the magnetization, we observe that despite acceptable agreement with the exact data for small values of a , sites 16, 18, and 19 exhibit larger errors compared to other sites, with a maximum absolute error of 0.096 (see Figure 20).

From the position of sites 16, 18 and 19, we hypothesize that interactions in the bulk are more difficult to capture, and so we conducted an additional simulation for a 19-site hexagon lattice (Figure 21), which has a configuration that is slightly bulkier than the 20-site ribbon lattice. Figures 22 and 23 present the results for the exact values and the differences between the exact and

TABLE III. Comparison of energy error, %RCE and F between QAOA, ADAPT-VQE, and the Max-Cut circuit introduced in this work for the frustrated 10-site ribbon Ising model with $a = 0.1$.

Method	Energy Error	%RCE	Fidelity	Gradient Threshold
QAOA	1.74323	-4107.5	0.067	-
ADAPT-VQE	0.00027	99.3	0.500	10^{-4} (3 iterations)
Max-Cut	0.00042	99.0	1.000	-

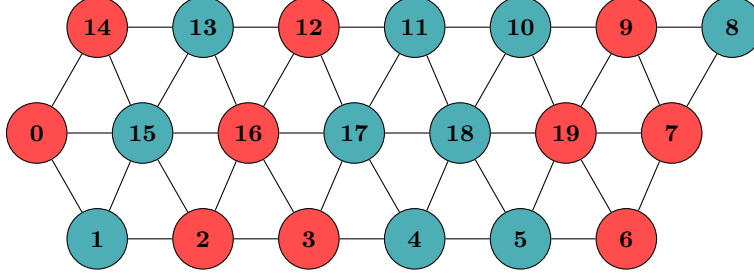
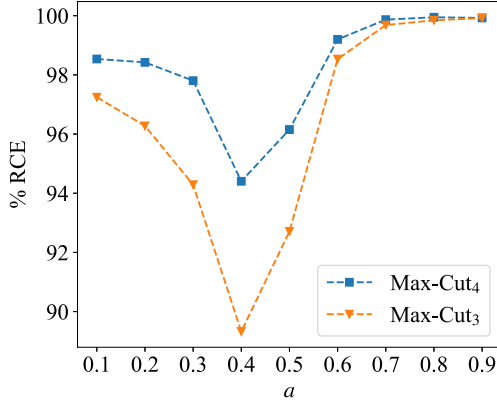
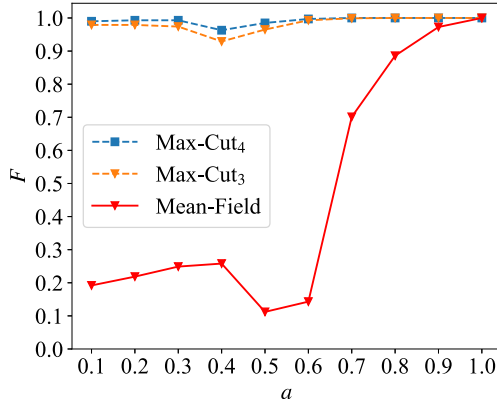


FIG. 15. One possible Max-Cut for the 20-site ribbon graph.



(a)



(b)

FIG. 16. %RCE for different m shown in (a), and F presented in (b) for the 20-site ribbon frustrated Ising model.

TABLE IV. Comparison of circuit complexity scaling for different methods across different system sizes.

Sites	Method	Depth	CNOT	Parameters
5	QAOA	310	216	36
	ADAPT-VQE(2)	161	98	59
	Max-Cut	31	30	15
10	QAOA	4701	3800	200
	ADAPT-VQE	551	342	194
	Max-Cut	121	168	84

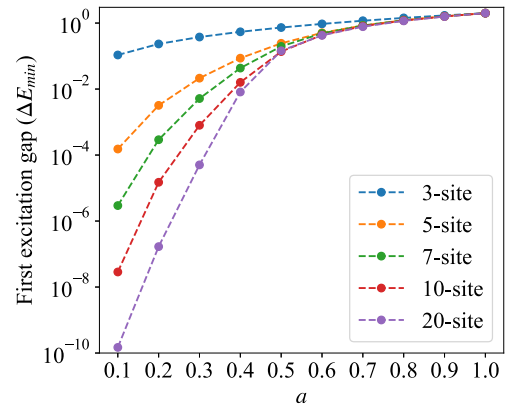


FIG. 17. First excitation gap for various lattice sizes and different values of a .

simulated results for $a = 0.1$, respectively. The output state fidelity is 0.972, with an energy error of 1.242×10^{-2} . The circuit complexity corresponding to the 19-site lattice is summarized in Table V. The results demonstrate that the proposed method successfully produces a state

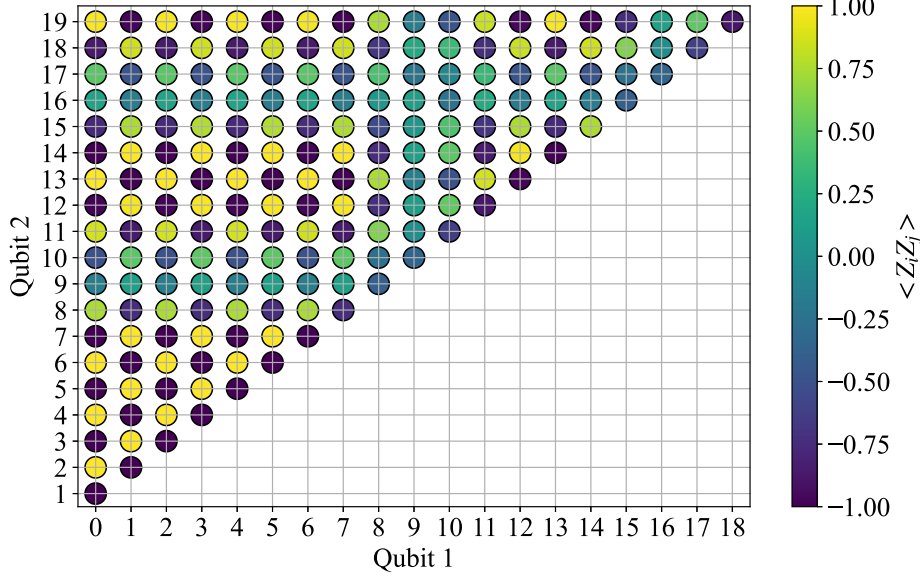


FIG. 18. The correlation function obtained from the exact results for the 20-site ribbon system.

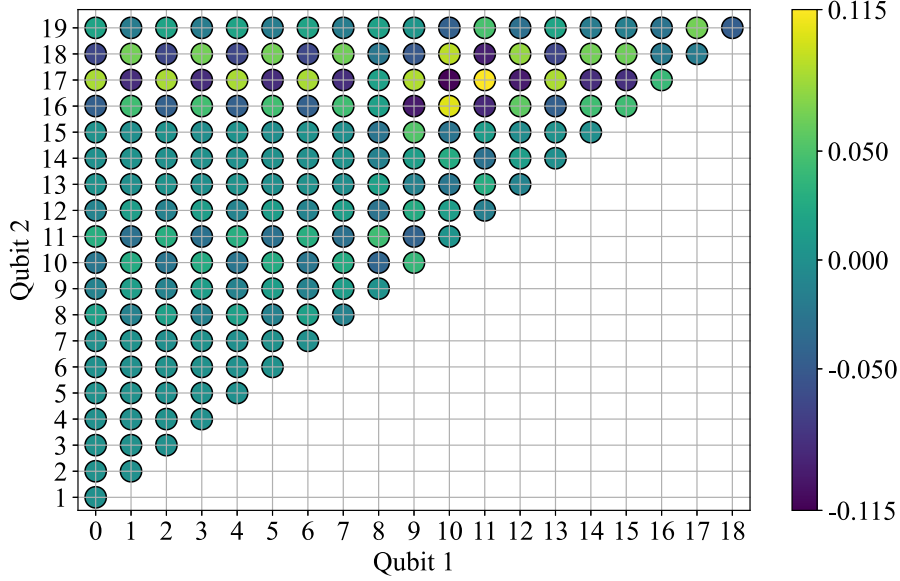


FIG. 19. The difference between the correlation function for the exact results and the simulated results for the 20-site ribbon system.

with high fidelity. Additionally, the correlation function derived from the simulation shows good agreement for most interactions. Notably, for site 9, which is located at the center of the graph and is farthest from the edges, the error in the correlation function involving this site is relatively low.

Moreover, the magnetization was calculated and compared to the exact result, as shown in Figure 24. The

values obtained from the circuit approximate the exact results well, with the highest absolute error being 0.083. As illustrated in Figure 24b, although sites 5 and 13 are expected to behave identically due to the lattice symmetry, the Max-Cut circuit breaks this symmetry, leading to a larger error at site 13 than 5.

TABLE V. Summary of the CNOT gate count and the number of parameters in the Max-Cut circuit for different system sizes, evaluated for $m = 3$.

Name	Sites (n)	CNOT	Parameters
House	5	30	15
Hexagon	7	108	54
Ribbon	10	168	84
Hexagon	19	360	180
Ribbon	20	360	180

III. CONCLUSION

We introduced a 2-qc block to design a variational quantum circuit for Ising spin glasses using the VQE framework. Graph partitioning of the underlying frustrated lattice based on the Max-Cut problem is utilized to minimize circuit depth. The method has been tested on frustrated lattices with up to 20 sites. Notably, when scaling the circuit from a 10-site to a 20-site lattice, the number of CNOT gates, circuit depth, and required parameters increases by a factor of 2, despite the exponential growth in the number of possible configurations, exceeding one million for the 20-site lattice. In the RVB picture, the number of possible pairings for a 20-site lattice exceeds 650 million, compared to only 945 pairings for a 10-site lattice. This demonstrates the exponential growth in circuit depth required to accommodate all possible pairings, highlighting the importance of methods that can reduce the search space by identifying significant pairings. By employing graph partitioning based on Max-Cut, the circuit complexity is significantly reduced.

In general, finding a Max-Cut is an NP-hard problem. The most effective classical polynomial-time approximation algorithm is that of Goemans and Williamson [87], which employs semidefinite programming combined with randomized rounding and achieves an approximation ratio of approximately 88% of the maximum cut. In comparison, the QAOA algorithm yields an approximation ratio of about 69%. Nevertheless, for planar graphs, classical polynomial-time methods exist that reformulate the Max-Cut problem as a maximum-weight matching problem solvable using polynomial-time algorithms [37].

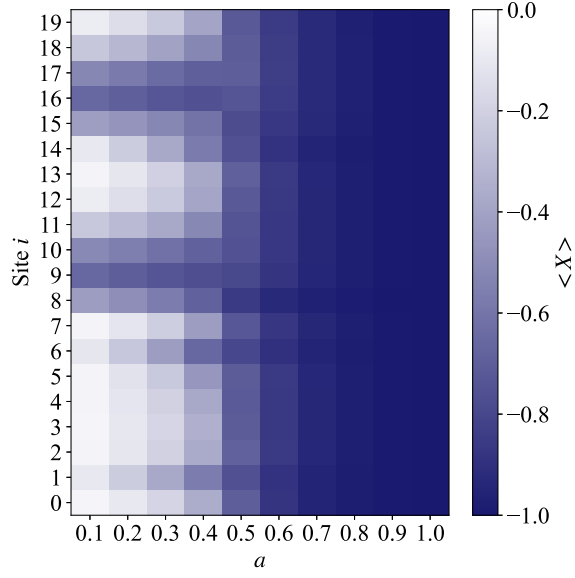
For an n -site planar graph with k edges determined by Max-Cut, the number of CNOT gates and parameters for a single layer of source and sink are $4k$ and $2k$, respectively. For m layers, the circuit requires $4mk$ CNOT gates and $2mk$ parameters. Based on the results, $m = 3$ provides acceptable accuracy compared to exact solutions, meaning that the circuit complexity also remains polynomial. It should be mentioned that the seemingly constant $m = 3$ was not tested on larger systems than 20 spins, because of computational limitations on the exact benchmark results, which require exact diagonalization in an exponentially scaling Hilbert space. However, if a constant or polynomially scaling m with

system size can be confirmed, the MaxCut circuit design might open a door to polynomial scaling simulation of RVB spin glasses on quantum devices.

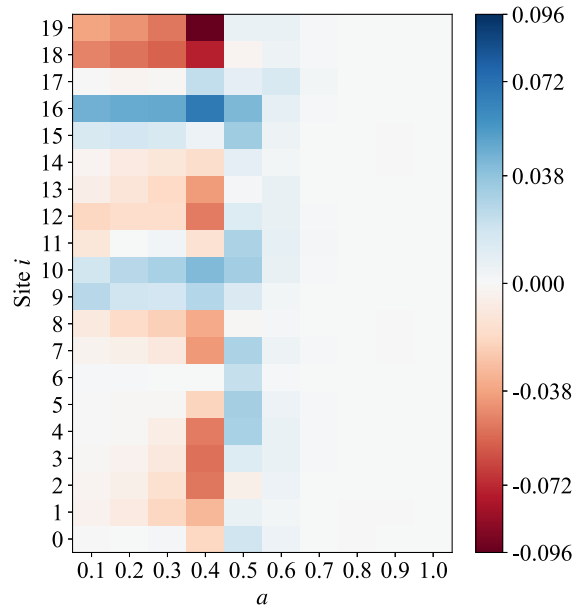
Finally, the 2-qc block exhibits a group structure, as this operation is closed for any input in the Hilbert space. Additionally, the commutation properties with the total-spin flip operator, such as the Hamiltonian of the problem, can provide potential insights by examining the corresponding Lie algebraic structure and the dynamical Lie algebra of the building block. This aspect will be addressed in future work.

ACKNOWLEDGMENTS

SDB and SEG acknowledge the Canada Research Chair program, the CFI, NSERC Discovery Grant program, and NBIF for financial support.



(a)



(b)

FIG. 20. The magnetization obtained from the exact results for the 20-site ribbon system is shown in (a), and the difference between the magnetization obtained from the exact results and the simulated results is shown in (b).

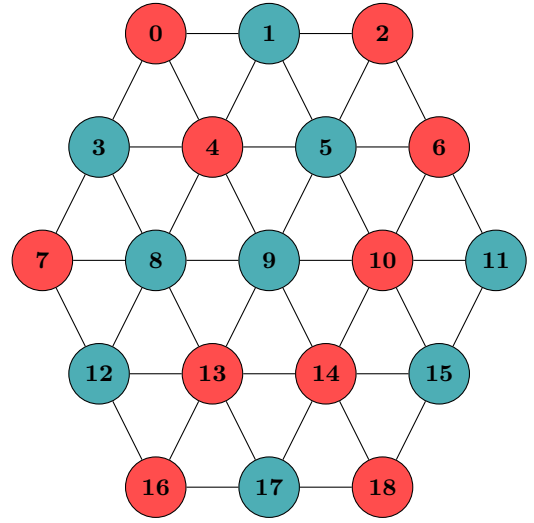


FIG. 21. One of the forty possible Max-Cut configurations for the 19-site hexagon graph.

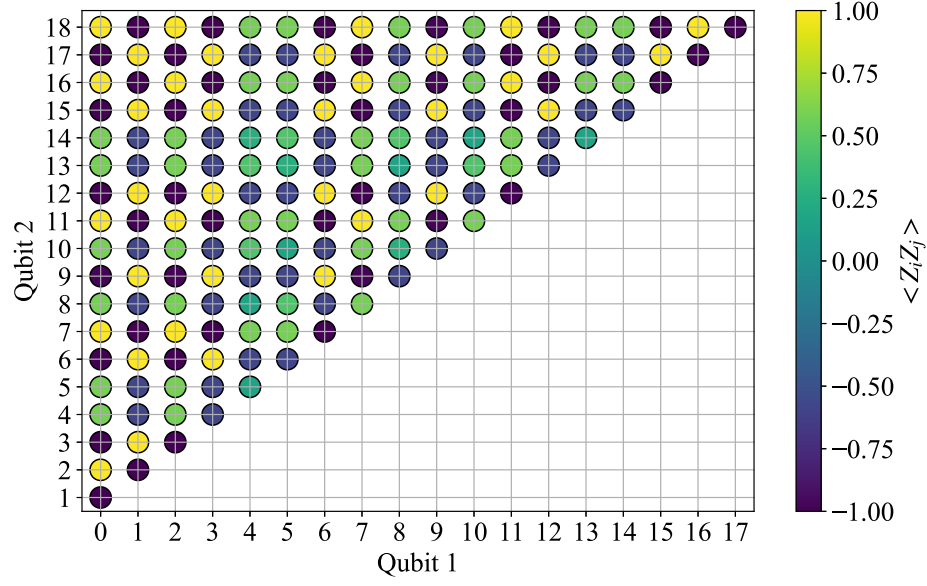


FIG. 22. The correlation function obtained from the exact results for the 19-site hexagon system.

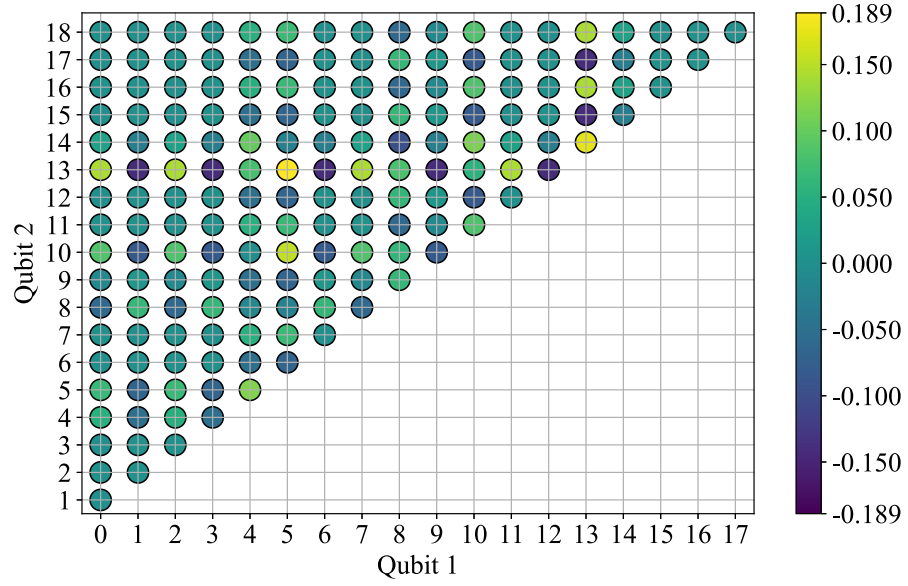
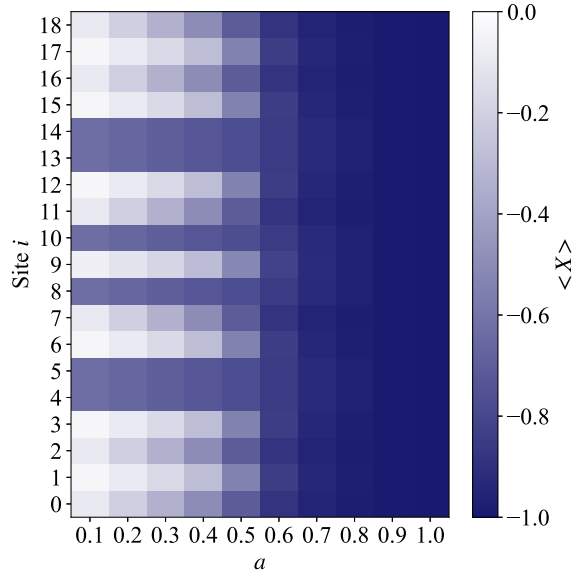
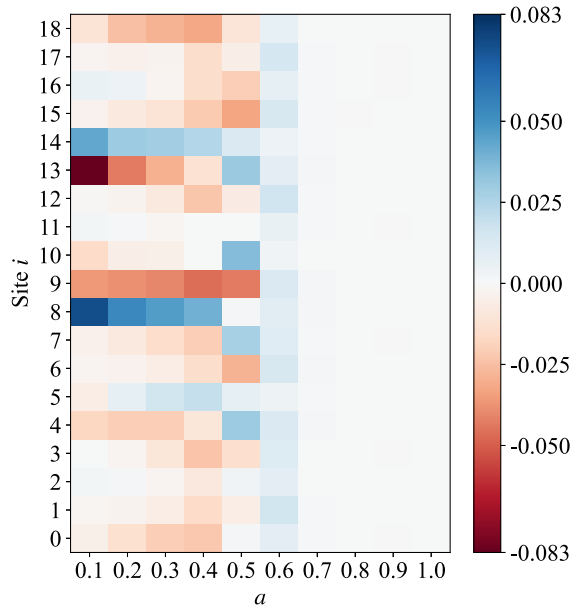


FIG. 23. The difference between the correlation function for the exact results and the simulated results for the 19-site hexagon system.



(a)



(b)

FIG. 24. The magnetization obtained from the exact results for the 19-site hexagon system is shown in (a), and the difference between the magnetization obtained from the exact results and the simulated results is shown in (b).

Appendix A: QAOA and ADAPT-VQE

In the QAOA approach to simulating the Ising model of spin glasses, the mixer Hamiltonian was chosen as $H_M = \sum_{i=0}^{n-1} Y_i$, and 18 layers of problem and mixer Hamiltonians were applied. For the ADAPT-VQE method, an operator pool was constructed using single-qubit and two-qubit gates to implement single and double excitations, representing spin flips at lattice sites. We have the following candidate operators for constructing the pool:

Single-Qubit Operators: $\{\sigma_i^\alpha\}$.

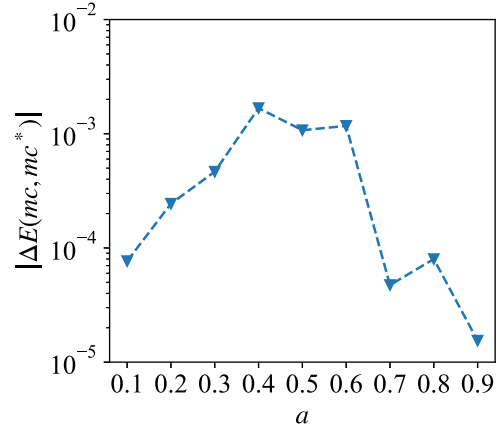
Two-Qubit Operators: $\{\sigma_i^\alpha \sigma_j^\beta\}$.

The two-qubit operators included in the pool are derived from neighbor-neighbor interactions based on the graph structure. The gradient of the energy with respect to each operator is initially evaluated for the two-qubit operators. The selected operators are then implemented in a quantum circuit, which is initialized in the vacuum state, with their parameters optimized. In the subsequent step, the gradient for a single operator is measured and added to the existing circuit, followed by re-optimizing all parameters within the circuit. This iterative process continues until the gradient threshold and convergence tolerance are achieved.

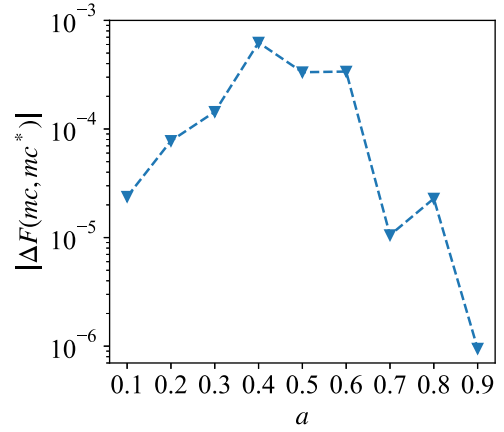
Appendix B: Comparative Analysis of Max-Cut Configurations (10-Site ribbon Lattice)

Here, we present a comparison between two distinct Max-Cut configurations in terms of energy error and fidelity for the 10-site ribbon lattice. We denote the configuration shown in Figure 12 as mc and the one in Figure 13 as mc^* . The energies obtained from the corresponding circuits for mc and mc^* are compared in Figure 25a. The absolute energy error, $|\Delta E(mc, mc^*)|$, demonstrates strong agreement between the two results, with the error remaining below 10^{-4} for $a = 0.1$, which represents the most challenging regime.

Furthermore, the difference in fidelity between the two output states, $\Delta F(mc, mc^*)$, with respect to the true ground state, has been computed and is shown in Figure 25b. The results indicate that the fidelity difference remains below 10^{-3} across the entire range of a , and notably below 10^{-4} for $a = 0.1$, suggesting that the two distinct Max-Cut configurations yield nearly identical output states.



(a)



(b)

FIG. 25. Comparison of two Max-Cut configurations in the 10-site ribbon lattice.

- [1] Samuel Frederick Edwards and Phil W Anderson. Theory of spin glasses. *Journal of Physics F: Metal Physics*, 5(5):965, 1975.
- [2] Paul Benioff. The computer as a physical system: A microscopic quantum mechanical hamiltonian model of computers as represented by turing machines. *Journal of Statistical Physics*, 22(5):563–591, May 1980.
- [3] Yuri Manin. Computable and uncomputable. *Sovetskoye Radio, Moscow*, 128:28, 1980.
- [4] Richard P Feynman. Simulating physics with computers. In *Feynman and computation*, pages 133–153. cRc Press, 2018.
- [5] A Yu Kitaev. Quantum measurements and the abelian stabilizer problem. *arXiv preprint quant-ph/9511026*, 1995.
- [6] Alexei Yu Kitaev, Alexander Shen, and Mikhail N Vyalyi. *Classical and quantum computation*. American Mathematical Soc., 2002.
- [7] Richard Cleve, Artur Ekert, Chiara Macchiavello, and Michele Mosca. Quantum algorithms revisited. *Proceedings of the Royal Society of London. Series A: Mathematical, Physical and Engineering Sciences*, 454(1969):339–354, 1998.
- [8] Michael A Nielsen and Isaac L Chuang. *Quantum computation and quantum information*, volume 2. Cambridge university press Cambridge, 2001.
- [9] Daniel S Abrams and Seth Lloyd. Quantum algorithm providing exponential speed increase for finding eigenvalues and eigenvectors. *Physical Review Letters*, 83(24):5162, 1999.
- [10] Alberto Peruzzo, Jarrod McClean, Peter Shadbolt, Man-Hong Yung, Xiao-Qi Zhou, Peter J Love, Alán Aspuru-Guzik, and Jeremy L O’Brien. A variational eigenvalue solver on a photonic quantum processor. *Nature communications*, 5(1):4213, 2014.
- [11] Jarrod R McClean, Jonathan Romero, Ryan Babbush, and Alán Aspuru-Guzik. The theory of variational hybrid quantum-classical algorithms. *New Journal of Physics*, 18(2):023023, 2016.
- [12] John Preskill. Quantum computing in the nisq era and beyond. *Quantum*, 2:79, 2018.
- [13] Lennart Bittel and Martin Kliesch. Training variational quantum algorithms is np-hard. *Physical review letters*, 127(12):120502, 2021.
- [14] Edward Farhi, Jeffrey Goldstone, and Sam Gutmann. A quantum approximate optimization algorithm. *arXiv preprint arXiv:1411.4028*, 2014.
- [15] Kostas Blekos, Dean Brand, Andrea Ceschini, Chiao-Hui Chou, Rui-Hao Li, Komal Pandya, and Alessandro Summer. A review on quantum approximate optimization algorithm and its variants. *Physics Reports*, 1068:1–66, 2024. A review on Quantum Approximate Optimization Algorithm and its variants.
- [16] Charles Moussa, Hao Wang, Thomas Bäck, and Vedran Dunjko. Unsupervised strategies for identifying optimal parameters in quantum approximate optimization algorithm. *EPJ Quantum Technology*, 9(1):11, 2022.
- [17] Joao Basso, Edward Farhi, Kunal Marwaha, Benjamin Villalonga, and Leo Zhou. The quantum approximate optimization algorithm at high depth for maxcut on large-girth regular graphs and the sherrington-kirkpatrick model. *arXiv preprint arXiv:2110.14206*, 2021.
- [18] Jaeho Choi and Joongheon Kim. A tutorial on quantum approximate optimization algorithm (qaoa): Fundamentals and applications. In *2019 international conference on information and communication technology convergence (ICTC)*, pages 138–142. IEEE, 2019.
- [19] Michael Streif, Sheir Yarkoni, Andrea Skolik, Florian Neukart, and Martin Leib. Beating classical heuristics for the binary paint shop problem with the quantum approximate optimization algorithm. *Physical Review A*, 104(1):012403, 2021.
- [20] Ajinkya Borle, Vincent Elfving, and Samuel J Lomonaco. Quantum approximate optimization for hard problems in linear algebra. *SciPost Physics Core*, 4(4):031, 2021.
- [21] Mark Hodson, Brendan Ruck, Hugh Ong, David Garvin, and Stefan Dulman. Portfolio rebalancing experiments using the quantum alternating operator ansatz. *arXiv preprint arXiv:1911.05296*, 2019.
- [22] Pontus Vikstål, Mattias Grönkvist, Marika Svensson, Martin Andersson, Göran Johansson, and Giulia Ferrini. Applying the quantum approximate optimization algorithm to the tail-assignment problem. *Physical Review Applied*, 14(3):034009, 2020.
- [23] Hasan Mustafa, Sai Nandan Morapakula, Prateek Jain, and Srinjoy Ganguly. Variational quantum algorithms for chemical simulation and drug discovery. In *2022 International Conference on Trends in Quantum Computing and Emerging Business Technologies (TQCEBT)*, pages 1–8. IEEE, 2022.
- [24] Kurt Binder and A Peter Young. Spin glasses: Experimental facts, theoretical concepts, and open questions. *Reviews of Modern physics*, 58(4):801, 1986.
- [25] Marc Mézard, Giorgio Parisi, and Miguel Angel Virasoro. *Spin glass theory and beyond: An Introduction to the Replica Method and Its Applications*, volume 9. World Scientific Publishing Company, 1987.
- [26] Marc Mezard and Andrea Montanari. *Information, physics, and computation*. Oxford University Press, 2009.
- [27] Daniel L Stein and Charles M Newman. *Spin glasses and complexity*, volume 4. Princeton University Press, 2013.
- [28] John A Mydosh. *Spin glasses: an experimental introduction*. CRC Press, 1993.
- [29] Vincent Cannella and John A Mydosh. Magnetic ordering in gold-iron alloys. *Physical Review B*, 6(11):4220, 1972.
- [30] CAM Mulder, AJ Van Duynveldt, and JA Mydosh. Susceptibility of the cu mn spin-glass: Frequency and field dependences. *Physical Review B*, 23(3):1384, 1981.
- [31] Caterina De Simone, Martin Diehl, Michael Jünger, Petra Mutzel, Gerhard Reinelt, and Giovanni Rinaldi. Exact ground states of ising spin glasses: New experimental results with a branch-and-cut algorithm. *Journal of Statistical Physics*, 80:487–496, 1995.
- [32] Francisco Barahona. On the computational complexity of ising spin glass models. *Journal of Physics A: Mathematical and General*, 15(10):3241, 1982.
- [33] Jack Edmonds. Minimum partition of a matroid into independent subsets. *J. Res. Nat. Bur. Standards Sect. B*, 69:67–72, 1965.
- [34] L Bieche, JP Uhry, R Maynard, and R Rammal. On the ground states of the frustration model of a spin glass by

- a matching method of graph theory. *Journal of Physics A: Mathematical and General*, 13(8):2553, 1980.
- [35] Francisco Barahona, Roger Maynard, Rammal Rammal, and Jean-Pierre Uhry. Morphology of ground states of two-dimensional frustration model. *Journal of Physics A: Mathematical and General*, 15(2):673, 1982.
- [36] JC Angles d’Auriac and R Maynard. On the random antiphase state in the $\pm j$ spin glass model in two dimensions. *Solid state communications*, 49(8):785–790, 1984.
- [37] Frank Hadlock. Finding a maximum cut of a planar graph in polynomial time. *SIAM Journal on Computing*, 4(3):221–225, 1975.
- [38] GI Orlova. Finding the maximum cut in a graph. *Engineering Cybernetics*, 10:502–506, 1972.
- [39] Caterina De Simone, Martin Diehl, Michael Jünger, Petra Mutzel, Gerhard Reinelt, and Giovanni Rinaldi. Exact ground states of two-dimensional $\pm j$ ising spin glasses. *Journal of Statistical Physics*, 84:1363–1371, 1996.
- [40] Uwe Gropengiesser. The ground-state energy of the $\pm j$ spin glass. a comparison of various biologically motivated algorithms. *Journal of Statistical Physics*, 79:1005–1012, 1995.
- [41] Uwe Gropengiesser. Superlinear speedup for parallel implementation of biologically motivated spin glass optimization algorithm. *International Journal of Modern Physics C*, 6(02):307–315, 1995.
- [42] Patrick Sutton and Sheri Boyden. Genetic algorithms: a general search procedure. *American Journal of Physics*, 62(6):549–552, 1994.
- [43] Francisco Barahona. Ground-state magnetization of ising spin glasses. *Physical Review B*, 49(18):12864, 1994.
- [44] Shoudan Liang. Application of cluster algorithms to spin glasses. *Physical review letters*, 69(14):2145, 1992.
- [45] Scott Kirkpatrick, C Daniel Gelatt Jr, and Mario P Vecchi. Optimization by simulated annealing. *science*, 220(4598):671–680, 1983.
- [46] Mark W Johnson, Mohammad HS Amin, Suzanne Gildert, Trevor Lanting, Firas Hamze, Neil Dickson, Richard Harris, Andrew J Berkley, Jan Johansson, Paul Bunyk, et al. Quantum annealing with manufactured spins. *Nature*, 473(7346):194–198, 2011.
- [47] Edward Farhi, Jeffrey Goldstone, Sam Gutmann, and Michael Sipser. Quantum computation by adiabatic evolution. *arXiv preprint quant-ph/0001106*, 2000.
- [48] J Brooke, David Bitko, Rosenbaum, and Gabriel Aeppli. Quantum annealing of a disordered magnet. *Science*, 284(5415):779–781, 1999.
- [49] Tadashi Kadowaki and Hidetoshi Nishimori. Quantum annealing in the transverse ising model. *Physical Review E*, 58(5):5355, 1998.
- [50] Giuseppe E Santoro, Roman Martonák, Erio Tosatti, and Roberto Car. Theory of quantum annealing of an ising spin glass. *Science*, 295(5564):2427–2430, 2002.
- [51] Massimo Bernaschi, Isidoro González-Adalid Pemartín, Víctor Martín-Mayor, and Giorgio Parisi. The quantum transition of the two-dimensional ising spin glass. *Nature*, pages 1–6, 2024.
- [52] Tim Bode and Frank K Wilhelm. Adiabatic bottlenecks in quantum annealing and nonequilibrium dynamics of paramagnons. *Physical Review A*, 110(1):012611, 2024.
- [53] Edward Farhi, David Gosset, Itay Hen, Anders W Sandvik, Peter Shor, A Peter Young, and Francesco Zamponi. Performance of the quantum adiabatic algorithm on random instances of two optimization problems on regular hypergraphs. *Physical Review A—Atomic, Molecular, and Optical Physics*, 86(5):052334, 2012.
- [54] Itay Hen and A Peter Young. Exponential complexity of the quantum adiabatic algorithm for certain satisfiability problems. *Physical Review E—Statistical, Nonlinear, and Soft Matter Physics*, 84(6):061152, 2011.
- [55] Sergey Knysh. Zero-temperature quantum annealing bottlenecks in the spin-glass phase. *Nature communications*, 7(1):12370, 2016.
- [56] Shu Tanaka, Ryo Tamura, and Bikas K Chakrabarti. *Quantum spin glasses, annealing and computation*. Cambridge University Press, 2017.
- [57] Frank Verstraete, J Ignacio Cirac, and José I Latorre. Quantum circuits for strongly correlated quantum systems. *Physical Review A—Atomic, Molecular, and Optical Physics*, 79(3):032316, 2009.
- [58] Alba Cervera-Lierta. Exact ising model simulation on a quantum computer. *Quantum*, 2:114, 2018.
- [59] Youngseok Kim, Andrew Eddins, Sajant Anand, Ken Xuan Wei, Ewout Van Den Berg, Sami Rosenblatt, Hasan Nayfeh, Yantao Wu, Michael Zaletel, Kristan Temme, et al. Evidence for the utility of quantum computing before fault tolerance. *Nature*, 618(7965):500–505, 2023.
- [60] Andrew D. King, Alberto Nocera, Marek M. Rams, Jacek Dziarmaga, Roeland Wiersema, William Bernoudy, Jack Raymond, Nitin Kaushal, Niclas Heinsdorf, Richard Harris, Kelly Boothby, Fabio Altomare, Mohsen Asad, Andrew J. Berkley, Martin Boschnak, Kevin Chern, Holly Christiani, Samantha Cibere, Jake Connor, Martin H. Dehn, Rahul Deshpande, Sara Ejtemaee, Pau Farre, Kelsey Hamer, Emile Hoskinson, Shuiyuan Huang, Mark W. Johnson, Samuel Kortas, Eric Ladizinsky, Trevor Lanting, Tony Lai, Ryan Li, Allison J. R. MacDonald, Gaelen Marsden, Catherine C. McGeoch, Reza Molavi, Travis Oh, Richard Neufeld, Mana Norouzpour, Joel Pasvolsky, Patrick Poitras, Gabriel Poulin-Lamarre, Thomas Prescott, Mauricio Reis, Chris Rich, Mohammad Samani, Benjamin Sheldon, Anatoly Smirnov, Edward Sterpka, Berta Trullas Clavera, Nicholas Tsai, Mark Volkmann, Alexander M. Whiticar, Jed D. Whittaker, Warren Wilkinson, Jason Yao, T.J. Yi, Anders W. Sandvik, Gonzalo Alvarez, Roger G. Melko, Juan Carrasquilla, Marcel Franz, and Mohammad H. Amin. Beyond-classical computation in quantum simulation. *Science*, 0(0):ead06285, 2025.
- [61] Andrew Lucas. Ising formulations of many np problems. *Frontiers in Physics*, 2, 2014.
- [62] Santo Fortunato. Community detection in graphs. *Physics Reports*, 486(3):75–174, 2010.
- [63] Richard A Goldstein, Zaida A Luthey-Schulten, and Peter G Wolynes. Optimal protein-folding codes from spin-glass theory. *Proceedings of the National Academy of Sciences*, 89(11):4918–4922, 1992.
- [64] John J Hopfield. Neural networks and physical systems with emergent collective computational abilities. *Proceedings of the national academy of sciences*, 79(8):2554–2558, 1982.
- [65] William A Little. The existence of persistent states in the brain. *Mathematical biosciences*, 19(1-2):101–120, 1974.
- [66] Daniel J Amit, Hanoach Gutfreund, and Haim Sompolinsky. Spin-glass models of neural networks. *Physical Review A*, 32(2):1007, 1985.
- [67] Haim Sompolinsky. Statistical mechanics of neural net-

- works. *Physics Today*, 41(12):70–80, 1988.
- [68] Dian Wu, Lei Wang, and Pan Zhang. Solving statistical mechanics using variational autoregressive networks. *Physical review letters*, 122(8):080602, 2019.
- [69] Mohamed Hibat-Allah, Estelle M Inack, Roeland Wiersema, Roger G Melko, and Juan Carrasquilla. Variational neural annealing. *Nature Machine Intelligence*, 3(11):952–961, 2021.
- [70] B McNaughton, MV Milošević, A Perali, and S Pilati. Boosting monte carlo simulations of spin glasses using autoregressive neural networks. *Physical Review E*, 101(5):053312, 2020.
- [71] Marylou Gabrié, Grant M Rotskoff, and Eric Vandeneijnden. Adaptive monte carlo augmented with normalizing flows. *Proceedings of the National Academy of Sciences*, 119(10):e2109420119, 2022.
- [72] Feng Pan, Pengfei Zhou, Hai-Jun Zhou, and Pan Zhang. Solving statistical mechanics on sparse graphs with feedback-set variational autoregressive networks. *Physical Review E*, 103(1):012103, 2021.
- [73] Aäron Van Den Oord, Nal Kalchbrenner, and Koray Kavukcuoglu. Pixel recurrent neural networks. In *International conference on machine learning*, pages 1747–1756. PMLR, 2016.
- [74] Qunlong Ma, Zhi Ma, Jinlong Xu, Hairui Zhang, and Ming Gao. Message passing variational autoregressive network for solving intractable ising models. *Communications Physics*, 7(1):236, 2024.
- [75] Kyle Mills, Pooya Ronagh, and Isaac Tamblyn. Finding the ground state of spin hamiltonians with reinforcement learning. *Nature Machine Intelligence*, 2(9):509–517, 2020.
- [76] Changjun Fan, Mutian Shen, Zohar Nussinov, Zhong Liu, Yizhou Sun, and Yang-Yu Liu. Searching for spin glass ground states through deep reinforcement learning. *Nature communications*, 14(1):725, 2023.
- [77] Qiskit contributors. Qiskit: An open-source framework for quantum computing, 2023.
- [78] Philip W Anderson. Resonating valence bonds: A new kind of insulator? *Materials Research Bulletin*, 8(2):153–160, 1973.
- [79] Seyed Ehsan Ghasempouri, Gerhard W. Dueck, and Stijn De Baerdemacker. Modular cluster circuits for the variational quantum eigensolver. *The Journal of Physical Chemistry A*, 127(39):8168–8178, 2023. PMID: 37729640.
- [80] Frauke Liers and Gregor Pardella. A simple max-cut algorithm for planar graphs. Technical report, Universität zu Köln, 2008.
- [81] Wei-Kuan Shih, Sun Wu, and Yue-Sun Kuo. Unifying maximum cut and minimum cut of a planar graph. *IEEE Transactions on Computers*, 39(5):694–697, 1990.
- [82] Frauke Liers and Gregor Pardella. Partitioning planar graphs: a fast combinatorial approach for max-cut. *Computational Optimization and Applications*, 51(1):323–344, 2012.
- [83] Michael Ragone, Bojko N Bakalov, Frédéric Sauvage, Alexander F Kemper, Carlos Ortiz Marrero, Martín Larocca, and M Cerezo. A lie algebraic theory of barren plateaus for deep parameterized quantum circuits. *Nature Communications*, 15(1):7172, 2024.
- [84] Wikipedia contributors. Maximum cut — Wikipedia, The Free Encyclopedia, 2024. [Online; accessed 7-April-2025].
- [85] Dieter Kraft. A software package for sequential quadratic programming. *Forschungsbericht- Deutsche Forschungs- und Versuchsanstalt für Luft- und Raumfahrt*, 1988.
- [86] Harper R Grimsley, Sophia E Economou, Edwin Barnes, and Nicholas J Mayhall. An adaptive variational algorithm for exact molecular simulations on a quantum computer. *Nature communications*, 10(1):3007, 2019.
- [87] Michel X Goemans and David P Williamson. Improved approximation algorithms for maximum cut and satisfiability problems using semidefinite programming. *Journal of the ACM (JACM)*, 42(6):1115–1145, 1995.